Available online at www.sciencedirect.com
SCIENCE DIRECT®
International Journal of Heat and Mass Transfer 48 (2005) 2601–2612
International Journal of HEAT and MASS TRANSFER
www.elsevier.com/locate/ijhmt

Enhancement of oxygen transfer in liquid lead and lead–bismuth eutectic by natural convection

Jian Ma [a], Peng Guo [a], Jinsuo Zhang [b], Ning Li [b], Bingmei M. Fu [a,*]

[a] *Department of Mechanical Engineering, University of Nevada, Las Vegas, 4505 Maryland Parkway, Box 454027, Las Vegas, NV 89154, United States*
[b] *Los Alamos National Laboratory, Mail Stop K764, MST-10, Los Alamos, NM 87544, United States*

Received 1 January 2005; received in revised form 31 January 2005
Available online 21 March 2005

Abstract

The present study carries out numerical analysis of the coupled natural convection and oxygen transfer of low-Prandtl-number (~0.02) liquid lead and lead–bismuth eutectic (LBE) for testing and calibrating low concentration level oxygen sensors. The analysis is performed on the two-dimensional coordinates in a rectangular container, where the fluid movement is laminar for the purpose of sensor test and calibration. The oxygen supply is from the cover gas at the top of the container. Natural convection and oxygen transfer are examined under three temperature boundary conditions: (a) heated from the lower part and cooled from the upper part of the sidewalls of the container; (b) heated from the sidewalls and cooled from the top of the container; (c) one sidewall heated and the opposing wall cooled. It is found that there are four, two and one convective circulation cells under conditions (a), (b), and (c), respectively. All these flows induced by the natural convection greatly enhance the oxygen transfer in the liquid metal. The most efficient one is under condition (b), in which it takes about 1000 s for the oxygen concentration in the whole field to reach ~90% of the input oxygen concentration from the top, instead of $\sim 10^6$ s by the pure diffusion.

Keywords: Oxygen transfer; Nature convection; Liquid metal

1. Introduction

Liquid lead or lead–bismuth eutectic (LBE) has been a primary candidate for high-power spallation neutron target and nuclear coolant due to its appropriate thermal–physical and chemical properties, such as low melting point, high thermal conductivity, and low vapor pressure [1]. However, lead alloys are very corrosive to common steels used in the nuclear installation [2]. This corrosion becomes a critical barrier in their applications. To reduce the corrosion, a protective oxide film needs to be built up at the interface of liquid metals and their steel carriers [3]. Unfortunately, it has been found that the pre-oxidation of steels does not prevent corrosion through the oxygen exchange in non-isothermal lead and bismuth systems based on the thermodynamic consideration [4]. Instead, a well-controlled extremely low oxygen concentration level (as low as 10^{-7} wt.% in

* Corresponding author. Current address: Department of Biomedical Engineering, The City College of the City University of New York, 138th Street at Convent Avenue, New York, NY 10031, United States. Tel.: +1 212 650 7531; fax: +1 212 650 6727.
E-mail address: fu@ccny.cuny.edu (B.M. Fu).

0017-9310/$ - see front matter © 2005 Elsevier Ltd. All rights reserved.
doi:10.1016/j.ijheatmasstransfer.2005.01.025

Nomenclature

c, C	oxygen concentration (kg/m^3) and dimensionless oxygen concentration
c_{max}	maximal oxygen concentration (kg/m^3), $C_{max} = 1$
D	oxygen diffusion coefficient (m^2/s)
g	gravity acceleration (m/s^2)
$\mathbf{g}$	gravity acceleration vector (m/s^2)
k	oxygen mass transfer coefficient (m/s)
L	characteristic length (m)
m_c	mean oxygen concentration in the container
p	pressure (Pa)
P_{O_2}	partial pressure of O_2
Pe	Peclet number, U_cL/α
Pr	Prandtl number, $\mu/(\rho\alpha)$
R	Universal gas constant (8.3144 J/mol/K)
Ra	Rayleigh number, $g\beta\Delta\theta L^3\rho/(\mu\alpha)$
Re	Reynolds number, $U_cL\rho/\mu$
Sc	Schmidt number, $\mu/(\rho D)$
Sh	local Sherwood number, $Sh = kL/D$
$\overline{Sh}$	average Sherwood number
t, T	time (s) and dimensionless time
t_d	diffusion time scale, L^2/D
u, U	velocity (m/s) and dimensionless velocity component in the x-axis
U_c	Characteristic velocity (m/s), $U_c = \sqrt{\beta gL(\theta_{high} - \theta_{low})}$
v, V	velocity (m/s) and dimensionless velocity component in the y-axis
$\mathbf{v}$, $\mathbf{V}$	velocity vector (m/s) and dimensionless velocity vector
x	horizontal coordinate (m)
X	dimensionless horizontal coordinate, $X = x/L$
y	vertical coordinate (m)
Y	dimensionless vertical coordinate, $Y = y/L$

Greek symbols

α	thermal diffusivity (m^2/s)
β	thermal expansion coefficient (K^{-1})
μ	dynamic viscosity (kg/m/s)
ρ	density (kg/m^3)
θ, Θ	temperature (°C) and dimensionless temperature, $\Theta = \frac{\theta-\theta_{low}}{\theta_{high}-\theta_{low}}$
θ_0	reference temperature (°C)
θ_g	gas temperature (°C)
θ_{high}	higher temperature set on boundary (°C)
θ_{low}	lower temperature set on boundary (°C)
ω, Ω	vorticity (s^{-1}) and dimensionless vorticity, $\Omega = (L/U_c)\omega$
ψ, Ψ	stream function (m^2/s) and dimensionless stream function

liquid Pb and 10^{-10} wt.% in liquid LBE) is crucial in avoiding the corrosion of lead-alloy carriers as well as in avoiding the formation of lead oxide contaminations [5]. In order to uniformly and quickly mix oxygen of such a low concentration with liquid lead or LBE under high temperatures (350 °C–above 700 °C) for nuclear coolant applications, we propose a new method of using natural convection to enhance the oxygen transfer in liquid metals instead of mechanical mixing methods [6]. To guide our design for new mixing apparatus, we first numerically simulate oxygen-mixing processes in a 2-D rectangular container under different temperature conditions to study the natural convection mixing characteristics and estimate the time for concentration equilibrium.

Numerous researchers have been investigating the natural convection heat and mass transfer in an enclosure for a variety of applications, such as crystal growth [7], cooling of electronic component [8], and glass melting [9]. Heat transfer in liquid metal driven by natural convection in a cavity has been of considerable interest in crystal growth, purification of material, and many other fields [7,10]. Chu et al. [11] appeared to be the first to study the natural convection heat transfer from a discrete heat source in a 2-D enclosure filled with air. Later, Chadwick et al. [12] carried out both numerical and experimental studies of heat transfer on the influence of discrete heat sources on natural convection in a rectangular enclosure filled with air. Selver et al. [7] investigated natural convection heat transfer of a liquid metal in vertical circular cylinders heated locally from the side. However, to our best knowledge, there is no study of mass transfer in liquid metal by natural convection. Viskanta et al. [13] studied the 3-D liquid metal flow in a cavity. This study demonstrated that the average Nusselt number calculated from a 2-D analysis can be used as a first approximation to predict heat transfer in a 3-D cavity for low-Prandtl-number fluids such as liquid metals. Therefore, we perform our numerical simulation based on a 2-D rectangular container.

Measuring oxygen concentration in high temperature (>350 °C) liquid lead or LBE can be achieved reliably with the solid electrolyte sensors [14]. A zirconia-based solid electrolyte sensor for the oxygen-concentration measurement in LBE has been developed by Darling and Li [6]. However, the characteristics of this sensor have not been well examined. One application of our current study is to design a well-controlled system for

calibrating and testing the sensor. A stable, uniform and extremely low oxygen concentration in the liquid lead or LBE is the first requirement. Due to the low oxygen diffusivity in LBE ($\sim 10^{-8}$ m^2/s at 500 °C) [15], the enhancement of oxygen transfer is necessary in this oxygen sensor calibration system. Mechanical oscillation and stirring methods have been tested and they failed to produce a stable and uniform oxygen concentration. In addition, it is difficult to predict the time for oxygen reaching the expected level in the bulk of liquid lead or LBE if using mechanical mixing methods.

In the present study, a numerical analysis of the natural convection of liquid metal flow, as well as the mass transfer is carried out for a simplified 2-D geometry. Three different temperature boundary conditions are applied for creating natural convection mixing. Oxygen is introduced from the top of the container by using cover-gas scheme, and the free surface boundary condition is used at the interface between the gases and the liquid metal. A static free surface is assumed for the laminar liquid metal flow. The local and average Sherwood numbers at the interface are examined to predict the oxygen transfer rate into the liquid metal for different Rayleigh numbers (Ra) and Schmidt numbers (Sc). Finally, the critical time to reach the uniform oxygen concentration is determined for each temperature boundary condition.

2. Mathematical formulation and numerical techniques

A simplified 2-D geometry for our experimental setup of containers in nuclear engineering applications is shown in Fig. 1. On top of the cylindrical container (or rectangular cross-section), the gas oxygen is imported from an O_2/He gas cylinder. The liquid metal fills a space of L by L. The momentum and heat transports are described by the following continuity, momentum and energy equations with the Boussinesq approximation,

$$\nabla \cdot \mathbf{v} = 0 \tag{1}$$

$$\frac{\partial \mathbf{v}}{\partial t} + (\mathbf{v}\cdot\nabla)\mathbf{v} = -\frac{1}{\rho}\nabla p - \beta(\theta-\theta_0)\mathbf{g} + \frac{\mu}{\rho}\nabla^2\mathbf{v} \tag{2}$$

$$\frac{\partial \theta}{\partial t} + (\mathbf{v}\cdot\nabla)\theta = \alpha\nabla^2\theta \tag{3}$$

where $\mathbf{v}$ is the flow velocity vector, p is the pressure, and θ is the temperature of LBE. θ_0 is the reference temperature that equals the lower temperature at the boundary, θ_{low}, in our study. $\mathbf{g}$ is the vector of gravity acceleration. β, ρ, μ and α are the thermal expansion coefficient, density, dynamic viscosity and thermal diffusivity, respectively. Table 1 [16] lists the values of these parameters for liquid lead and LBE at 500 °C.

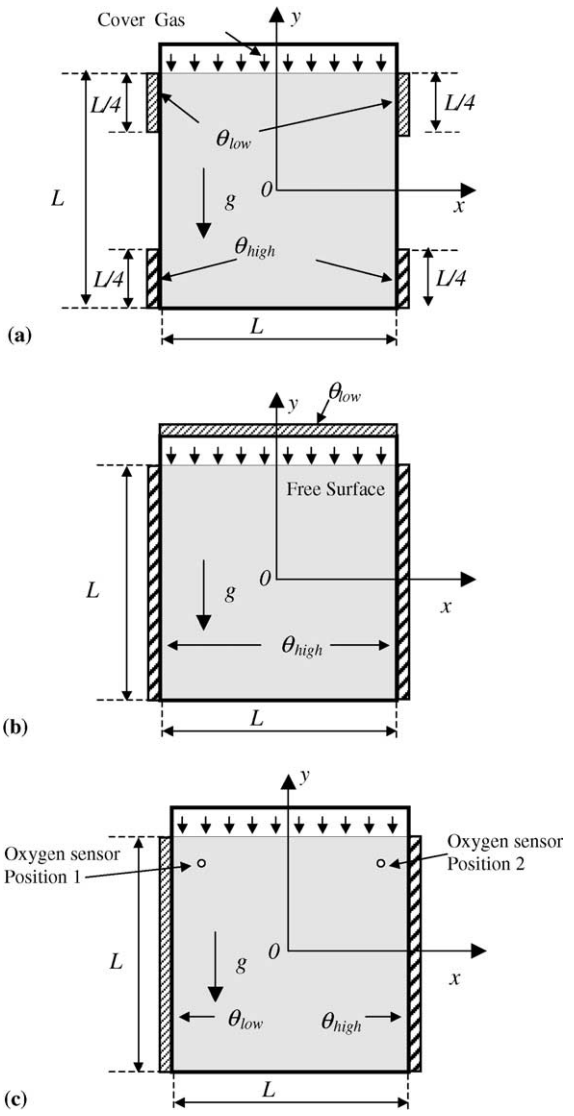

Fig. 1. Schematic of the simplified geometry for our container. Three temperature boundary conditions are considered. (a) Higher temperature heaters are at bottom sidewalls and lower temperature heaters are at top sidewalls. (b) Higher temperature heaters are at sidewalls and a lower temperature heater at the top. (c) A higher temperature heater is at the right sidewall and a lower temperature heater at the left sidewall. Places without heaters are insulated. Oxygen input is from the cover gases at the top of the container. Two oxygen sensors are located at the upper region of the container, which are $0.15L$ to the sidewall and $0.15L$ to the free surface of liquid metal, respectively.

For laminar and incompressible flow, the vorticity equation of flow can be written as:

$$\frac{\partial \omega}{\partial t} + (\mathbf{v}\cdot\nabla)\omega = \beta g\frac{\partial \theta}{\partial x} + \frac{\mu}{\rho}\nabla^2\omega \tag{4}$$

Table 1
Properties of liquid lead and lead–bismuth eutectic at 500 °C [16]

	Liquid lead	Liquid LBE
Density ρ (kg/m^3)	1.0476e4	1.012e4
Dynamic viscosity μ (kg/m/s)	1.833e−3	1.376e−3
Thermal diffusivity α (m^2/s)	1.003e−5	9.889e−6
Thermal expansion coefficient β (K^{-1})	1.116e−4	1.151e−4
Prandtl number Pr	1.75e−2	1.37e−2

If the length, velocity and time are scaled by L, $U_c = \sqrt{\beta g L(\theta_{high} - \theta_{low})}$, and $\frac{L}{\sqrt{\beta g L(\theta_{high}-\theta_{low})}}$, respectively, Eq. (4) becomes,

$$\frac{\partial \Omega}{\partial T} + (\mathbf{V}\cdot\nabla)\Omega = \frac{\partial \Theta}{\partial X} + \frac{1}{Re}\nabla^2\Omega \tag{5}$$

Here $\Omega = (L/U_c)\omega$ is the dimensionless vorticity. g is the gravity acceleration. L is the characteristic length, which is the width of container. $Re = U_c L\rho/\mu$ is the Reynolds number. $\Theta = (\theta - \theta_{low})/(\theta_{high} - \theta_{low})$ is the dimensionless temperature. θ_{high} and θ_{low} are the higher and lower temperatures at the boundaries (see Fig. 1). In our 2-D and incompressible case, Ω can be expressed as

$$\Omega = -\left(\frac{\partial^2 \Psi}{\partial X^2} + \frac{\partial^2 \Psi}{\partial Y^2}\right) \tag{6}$$

Ψ is the dimensionless stream function,

$$U = \frac{\partial \Psi}{\partial Y} \tag{7}$$

$$V = -\frac{\partial \Psi}{\partial X} \tag{8}$$

where $U = u/U_c$ and $V = v/U_c$ are the dimensionless velocity components along the x and y directions, respectively.

Eq. (3) can be written in the following dimensionless form,

$$\frac{\partial \Theta}{\partial T} + (V\cdot\nabla)\Theta = \frac{1}{Pe}\nabla^2\Theta \tag{9}$$

$Pe = Re\,Pr = (U_c L\rho/\mu) * (\mu/(\rho\alpha)) = U_c L/\alpha$, is the Peclet number for the heat transfer. $Pr = \mu/(\rho\alpha)$ is the Prandtl number.

The calculation domain is shown in Fig. 1. Non-slip boundary conditions are applied on the sidewalls of the rectangular container, while free surface condition is assumed at the interface of the cover gases and the liquid metal. Three different temperature boundary conditions are considered, as shown in Fig. 1(a)–(c), respectively. At the hotter boundary, dimensionless temperature $\Theta = 1$ and at the colder boundary, dimensionless temperature $\Theta = 0$. At other boundaries without heaters, adiabatic conditions are satisfied.

In summary, the boundary conditions for solving the flow and heat transfer problems are,

$$X = \pm 0.5, \quad -0.5 \leqslant Y \leqslant 0.5, \quad U = V = 0$$
(impermeable and non-slip conditions) (10)

$$Y = -0.5, \quad -0.5 \leqslant X \leqslant 0.5, \quad U = V = 0$$
(impermeable and non-slip conditions) (11)

$$Y = 0.5, \quad -0.5 < X < 0.5, \quad V = 0; \quad \frac{\partial U}{\partial Y} = 0$$
(free surface) (12)

For case (a), the temperature boundary conditions are,

$$X = \pm 0.5, \quad 0.25 \leqslant Y \leqslant 0.5, \quad \Theta = 0 \tag{13}$$

$$X = \pm 0.5, \quad -0.5 \leqslant Y \leqslant -0.25, \quad \Theta = 1 \tag{14}$$

$$X = \pm 0.5, \quad -0.25 < Y < 0.25, \quad \frac{\partial \Theta}{\partial X} = 0 \tag{15}$$

$$Y = \pm 0.5, \quad -0.5 < X < 0.5, \quad \frac{\partial \Theta}{\partial Y} = 0 \tag{16}$$

For case (b),

$$X = \pm 0.5, \quad -0.5 \leqslant Y \leqslant 0.5, \quad \Theta = 1 \tag{17}$$

$$Y = 0.5, \quad -0.5 < X < 0.5, \quad \Theta = 0$$
(Because the cover gas layer is narrow, it is approximated that the temperature at the liquid surface equals to that of the top of the enclosure.) (18)

$$Y = -0.5, \quad -0.5 < X < 0.5, \quad \frac{\partial \Theta}{\partial Y} = 0 \tag{19}$$

For case (c),

$$X = 0.5, \quad -0.5 \leqslant Y \leqslant 0.5, \quad \Theta = 1 \tag{20}$$

$$X = -0.5, \quad -0.5 \leqslant Y \leqslant 0.5, \quad \Theta = 0 \tag{21}$$

$$Y = \pm 0.5, \quad -0.5 < X < 0.5, \quad \frac{\partial \Theta}{\partial Y} = 0 \tag{22}$$

Holman [17] found that for the free-convection flow in an enclosed space, in order to form the laminar flow regimes for the vertical convection layer, the Rayleigh number Ra ($Ra = g\beta\Delta\theta L^3\rho/(\mu)$) should be $\leqslant 10^6$. We chose temperature difference $\Delta\theta = \theta_{high} - \theta_{low} =$ 0.005 °C, 0.017 °C, 0.04 °C, and 0.08 °C for $L = 0.1$ m (or other length and temperature difference combinations). $\theta_{low} = 500$ °C. These correspond to four Rayleigh numbers for the liquid lead: $Ra = 3116.3$, 10,595.6, 24,930.7, and 49,861.0, which are less than 10^6. Therefore, the liquid metal flows are all laminar in our cases.

According to the estimate of Zhang and Li [15] by using Stokes–Einstein equation, the oxygen diffusion

coefficient in the liquid lead or LBE, D, is $\sim 10^{-8}$ m^2/s at 500 °C. The characteristic diffusion time t_d ($=L^2/D$) is introduced to represent the diffusion time scale that describes the duration of full oxygen admixture by a pure diffusion [18]. t_d is $\sim 10^6$ s in our case if $L = 0.1$ m. Compared to the oxygen diffusion time, the time needed to reach the steady state for velocity ($L/U_c \sim 13$ s) and temperature ($L^2/\alpha \sim 100$ s) can be neglected. Therefore, the unsteady terms in Eqs. (2)–(4) and corresponding dimensionless equations can be neglected.

After calculating the steady-state temperature and flow fields, we solve the following unsteady mass transfer problem. In the experiment, the oxygen is introduced at the top of the liquid metal after the temperature and the flow achieve the steady state. The dissolving oxygen concentration at the liquid surface is assumed to be a constant, c_{max}. The dimensionless equation for oxygen transfer is,

$$\frac{\partial C}{\partial t} + (\mathbf{V}\cdot\nabla)C = \frac{1}{Re\,Sc}\nabla^2 C \tag{23}$$

where C is the dimensionless oxygen concentration, $C = c/c_{max}$. c is oxygen concentration. Sc is Schmidt number defined as $Sc = \mu/(\rho D)$. Three Schmidt numbers ($Sc = 8.75$, 17.5 and 35.0) are tested, corresponding to three oxygen diffusivities, $D = 0.5\times10^{-8}$, 1×10^{-8}, and 2×10^{-8} m^2/s. The boundary and initial conditions for the oxygen transfer are,

$$Y = 0.5, \quad -0.5 \leqslant X \leqslant 0.5, \quad C = 1 \tag{24}$$

$$Y = -0.5, \quad -0.5 \leqslant X \leqslant 0.5, \quad \frac{\partial C}{\partial Y} = 0 \tag{25}$$

$$X = \pm 0.5, \quad -0.5 < Y < 0.5, \quad \frac{\partial C}{\partial X} = 0 \tag{26}$$

$$T = 0, \quad -0.5 \leqslant X \leqslant 0.5, \quad -0.5 \leqslant Y < 0.5 \quad C = 0 \tag{27}$$

Here $T = t/t_d$ is the dimensionless time. The alternating-direction implicit (ADI) scheme is used for vorticity, energy and mass transfer equations. The simultaneous over-relaxation (SOR) approach is applied for the solution of stream function Ψ. To achieve the convergent result, the first-order upwind scheme is used for inertial term [19] for a low-Prandtl-number liquid. In order to avoid the instability of calculation for Eq. (23) with extremely low diffusivity, the hybrid method is employed [20].

Local and average Sherwood numbers, $Sh(X,T)$ and $\overline{Sh} = \int_{-0.5}^{0.5} Sh(X,T)|_{Y=0.5}\,dX$, are used to characterize the oxygen transfer at the gas and liquid interface. $Sh = kL/D$, k is the oxygen mass transfer coefficient at the liquid surface, L is the characteristic length of the container and D is the oxygen diffusivity in the liquid. From the conservation of mass at the gas and liquid interface, Sherwood number can be derived as,

$$Sh(X,T) = \frac{1}{1 - C_{bulk}(T)}\left.\frac{\partial C}{\partial Y}\right|_{Y=0.5} \tag{28}$$

Here $C_{bulk}(T)$ is the average or mean dimensionless concentration in the container at time T. $C_{bulk}(T)$ is defined as:

$$C_{bulk}(T) = \frac{\int_{-0.5}^{0.5}\int_{-0.5}^{0.5} C(X,Y,T)\,dX\,dY}{\int_{-0.5}^{0.5}\int_{-0.5}^{0.5} dX\,dY} \tag{29}$$

The computational code for this problem was validated for natural convection flow by an analytical result reported in [21,22]. In order to verify the mesh and time-step independency, the calculations were repeated on 100×100, 120×120 and 140×140 grids in the x and y directions. According to "heuristic" stability condition,

$$\frac{U^2\,\Delta T}{2} \leqslant \frac{1}{Re\,Sc} \tag{30}$$

the dimensionless time steps of 10^{-3}, 10^{-4} and 10^{-5} are selected for the mass transfer problem. There are only negligible changes on mass, flow and temperature distributions for different mashes and time steps. Therefore, the results presented here are referred to 100×100 grids (for both convection and mass transfer equations) and the dimensionless time step of 10^{-3} for mass transfer equation.

3. Results and discussion

3.1. Flow patterns and temperature distribution

The steady-state velocity distributions and isotherms are demonstrated in Fig. 2 for three temperature boundary conditions shown in Fig. 1 at $Ra = 3116.3$. Similar patterns are shown at higher Ra. From the velocity vector plots, we can see that there are four vortical cells in the container for case (a) when the bottom sidewalls are heated and the top sidewalls are cooled. There are two vortical cells for case (b) when the sidewalls are heated and the top wall is cooled. When one sidewall is heated and another sidewall is cooled, as in case (c), there is only one vortical cell in the container. The dimensionless velocity scale of 0.1 is shown at the top right of each plot. The velocity vector represents the magnitude of the flow velocity as well as its direction at local positions. The flow directions at the interfaces between adjacent vortical cells are identical in cases (a) and (b). These virtual interfaces separate the vortical cells. For cases (a) and (b), although the convection inside the vortical cells is strong, the convection between vortical cells is small. This observation will be further demonstrated in Fig. 5.

Higher values of flow velocity would result in more and quicker convective heat and mass transfer. When $Ra = 3116.3$, for case (a), the maximal dimensionless velocity of the upper flow is 0.0697, while the lower flow

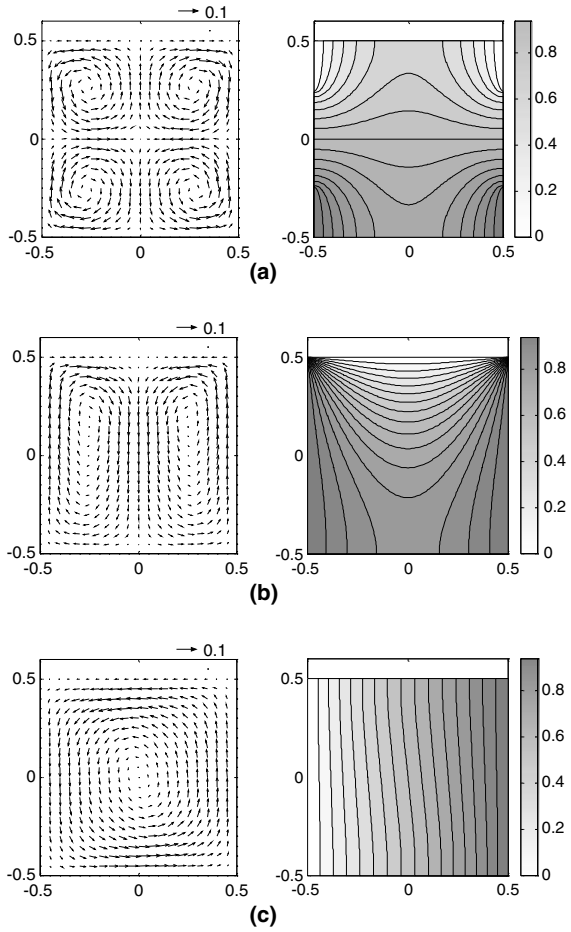

Fig. 2. Velocity field (left panel) and isotherms (right panel) of the convection flow under temperature boundary conditions (a), (b) and (c) at $Ra = 3116.3$.

has the maximal dimensionless velocity of 0.0690, which is slightly smaller than that of the upper fluid. This is due to a non-slip boundary condition at the bottom while a free surface boundary condition at the top of the enclosure. For case (b), the maximal dimensionless flow velocity in the container is 0.1136, which is about twice as much as that in case (a). The maximal dimensionless flow velocity in the container is 0.1830 under case (c), which is the highest among all three cases. This indicates that temperature boundary condition (c) is the most efficient way to enhance the flow convection, compared to conditions (a) and (b). As expected for case (c), the fluid flows from the hotter wall to the colder wall in the upper part of the enclosure, while flows from the colder wall to the hotter wall at the lower part of the enclosure. Subsequently, the isotherm distributions are distorted due to the intensive convection flow.

It is noticed that the flow velocity increases with *Ra* number due to higher natural convection. As shown in

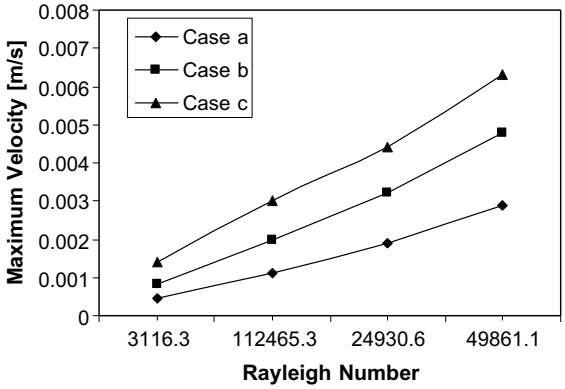

Fig. 3. Maximal flow velocities in the container for temperature boundary conditions (a), (b) and (c) as a function of Rayleigh number *Ra*.

Fig. 3, the maximal velocity in the enclosure increases with *Ra* number for all cases (a), (b) and (c). The increasing curves for each case are almost linear and parallel to each other. When *Ra* is from 3116.3 to 498614.4, a 16-fold increase, the maximal velocity in the enclosure increases 4.5-, 5.7- and 6.2-folds for cases (a), (b) and (c), respectively.

In Fig. 4, we plot the detailed velocity distributions at representative locations and their changes as *Ra* increases. Panels on the left side of Fig. 4 show the vertical velocity v at $Y = \pm 0.25$, while panels on the right side of Fig. 4 show the horizontal velocity u at the free surface, $Y = 0.5$ (see Fig. 1). Fig. 4(a)–(c) are for cases (a), (b) and (c), respectively. In all cases, the magnitudes of both velocity components increase with *Ra*, but at different rates.

3.2. Oxygen transport

Oxygen transport is studied under different Rayleigh numbers (*Ra*) and Schmidt numbers (*Sc*). The instantaneous oxygen concentration distributions at several time moments ($t = 41.9$ s, 298.8 s, 609.8 s and 1001.8 s) are illustrated in Fig. 5(a)–(c) for temperature boundary conditions (a), (b) and (c), at $Ra = 3116.3$ and $Sc = 17.5$ (corresponding to the values of μ, ρ for liquid lead in Table 1 and oxygen diffusion coefficient $D = 1 \times 10^{-8}$ m^2/s). The concentration contours at $t \geqslant 298.8$ s for each case are similar to their velocity distributions shown in Fig. 2. This clearly shows that natural convection is the dominant driving force for oxygen transfer. At $t = 41.9$ s, it is noted that oxygen only spreads to the upper part of the container from the free surface under temperature boundary condition (a). As time increases, oxygen starts to transfer from the upper part to the lower part and fills entire region of the container. There are four distinct regions for oxygen transport that

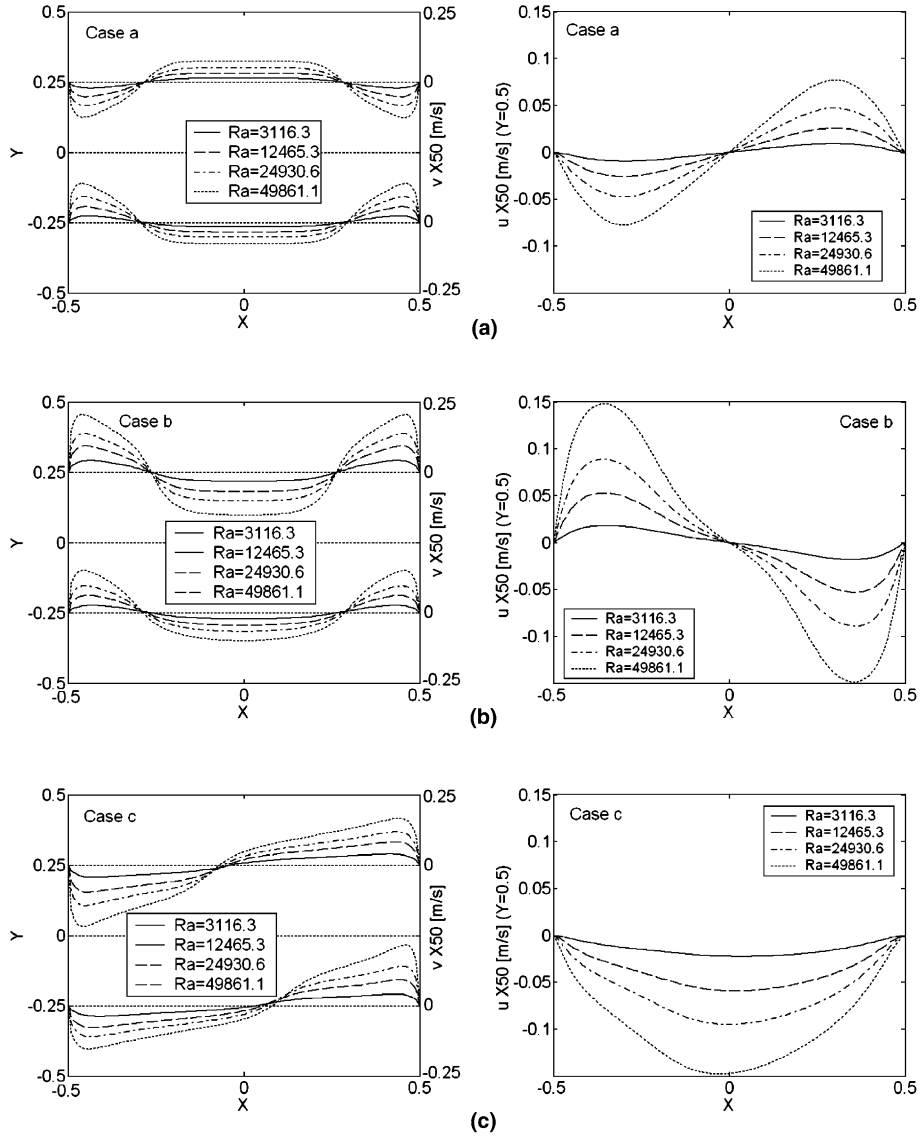

Fig. 4. Right panels: vertical velocity v at locations $Y = \pm 0.25$; Left panels: Horizontal velocity u at free surface for $Ra = 3116.3$, 10,595.3, 24,930.6, and 49,861.1 under temperature boundary conditions (a), (b) and (c). The velocity amplitudes are enlarged by 50 times with unit of m/s.

are similar to velocity fields. Under condition (b), the oxygen starts to transfer from the surface to the middle of the container, then to the bottom of enclosure and goes up from the sidewalls. There are two distinct regions for oxygen transport similar to velocity fields. Under condition (c), oxygen is carried by the convection flow to the left sidewall first and then towards the right. There is only one distinct region in the concentration field as in the velocity field.

Fig. 6(a)–(c) show the bulk (mean or average) oxygen concentration C_{bulk} (Eq. (29)) of the liquid metal as a function of time under three temperature boundary conditions (a), (b) and (c), when $Sc = 17.5$ and $Ra = 3116.3$, 12,465.3, 24,930.6 and 498,614.4, respectively. Fig. 6 explicitly shows that the higher Ra, or higher natural convection, the quicker the mixing and the larger the bulk oxygen concentration in the container. Of these three temperature boundary conditions, case (b) seems to be the best for oxygen transfer. This is more clearly shown in Fig. 7.

Fig. 7(a)–(c) compare the bulk oxygen concentration C_{bulk} rising in the liquid metal under three temperature boundary conditions when $Ra = 3116.3$ and $Sc = 8.75$, 17.5 and 35.0. For all Sc values, C_{bulk} in case (b) is the

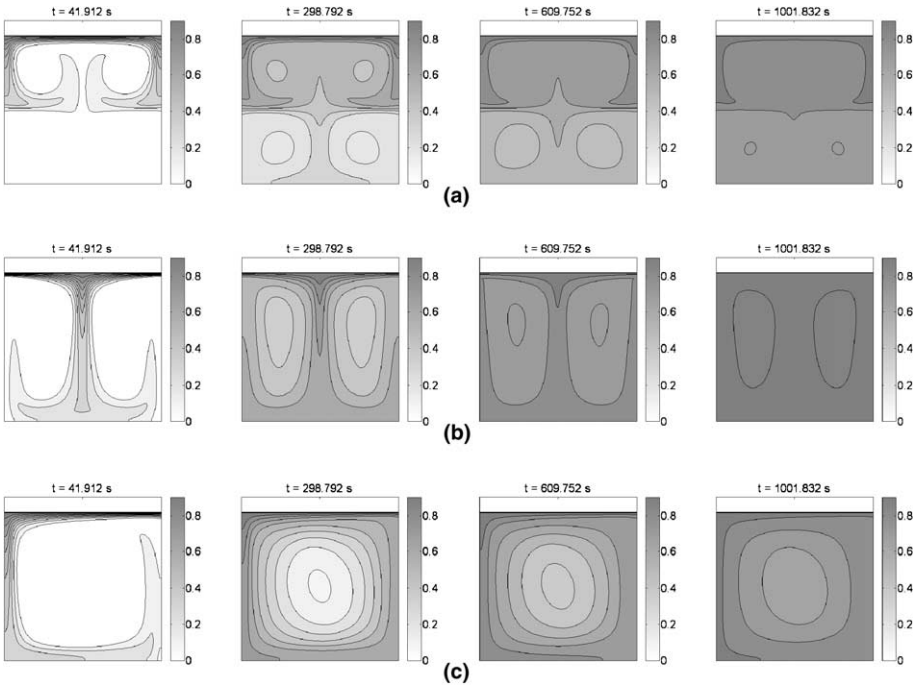

Fig. 5. Concentration contours at different times (t = 41.9, 298.8, 609.8 and 1001.8 s): (a) for temperature boundary condition (a), (b) for temperature boundary condition (b), (c) for temperature boundary condition (c). Ra = 3116.3 and Sc = 17.5 for all cases.

highest. In addition, case (b) is the fastest to reach the concentration equilibrium and therefore is the most efficient heating method to enhance the oxygen transfer in the liquid metal of our system. The difference in $C_{\text{bulk}}(t)$ for cases (a) and (c) is very small. The smaller the Sc (higher the oxygen diffusion coefficient D), it is faster for the concentration to reach equilibrium in each case. For example, in case (b) when Sc = 8.75 for oxygen diffusion coefficient D of 2×10^{-8} m^2/s, it takes about 600 s for reaching concentration equilibrium, while ~1000 s when Sc = 17.5 for $D = 10^{-8}$ m^2/s. This suggests that diffusion also plays a role in oxygen mixing under our conditions.

To quantify the oxygen transfer through our system, we plot the local and average Sherwood numbers at the free surface (Y = 0.5) in Fig. 8(a)–(c) for the same Sc (Sc = 17.5) but different Ra under temperature boundary conditions (a), (b) and (c). Left panel in Fig. 8 demonstrates the local Sherwood number $Sh(X,t)$ (Eq. (28)) as a function of location X at time t = 33.8 s. Right panel is for the average Sherwood number $\overline{Sh}(t)$ over $-0.5 < X < 0.5$ as a function of time t. For all cases, increasing Ra increases Sherwood number Sh and increases the oxygen transfer from the cover gas to the liquid metal. Although the distribution patterns for local Sherwood numbers appear largely different for cases (a), (b) and (c) at t = 33.8 s, the overall oxygen transfer through the free surface is similar. Under Ra = 3116.3, 10,595.6, 24,930.7, and 49,861.0, $\overline{Sh}(t = 33.8\text{ s}) = 12.1$, 23.9, 31.5, and 38.4 for case (a), $\overline{Sh}(t = 33.8\text{ s}) = 14.7$, 33.2, 44.0, and 53.4 for case (b) and $\overline{Sh}(t = 33.8\text{ s}) =$ 10.5, 19.2, 25.0 and 28.0 for case (c). The larger the Sherwood number, the larger the mass transfer is. Therefore, we find that case (b) is the best, case (a) is the second and case (c) is the worst method for oxygen mixing in our system although in case (c), the maximal velocity is the largest. Case (c) is the best for enhancing natural convection flow for liquid metals. For all cases, the average Sherwood numbers drop significantly with time. They almost reach steady values in about 100 s. This indicates that most oxygen enters the liquid metal from the free surface in less than 100 s after the cover gases are introduced at the top of the container.

To test and calibrate oxygen sensors, two oxygen sensors will be placed at the upper region of the container, as shown in Fig. 1 ($X = \pm0.35$, Y = 0.35). The time history of the oxygen concentration at two sensor locations is illustrated in Fig. 9 for different Sc numbers at Ra = 3116.3 under temperature boundary conditions (a), (b) and (c). It is found that at those positions, oxygen concentration reaches $c_{\max}$ (C = 1) faster under condition (b) than under the other two conditions as (b) is the best case for oxygen mixing.

Overlapping of the oxygen concentration curves at positions 1 and 2 (only a very subtle difference) as they should be due to symmetry in cases (a) and (b) validates

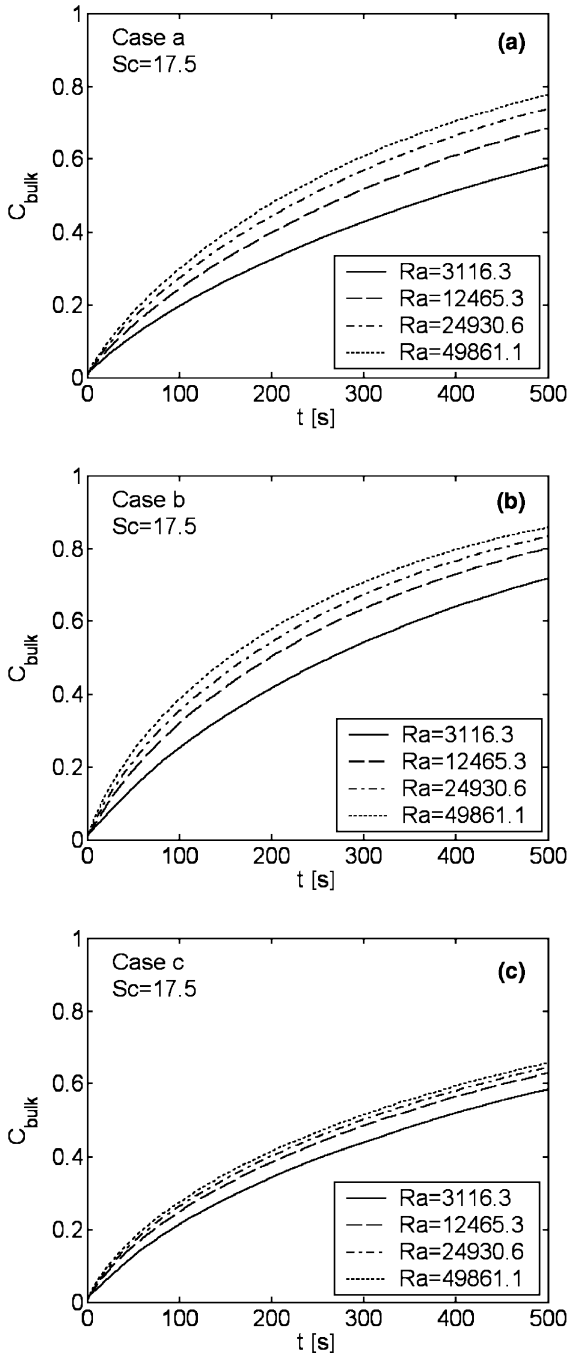

Fig. 6. The bulk (mean or average) oxygen concentration in the liquid as a function of time for temperature boundary conditions (a), (b) and (c) at $Sc = 17.5$ for $Ra = 3116.3$, 10,595.3, 24,930.6, and 49,861.1.

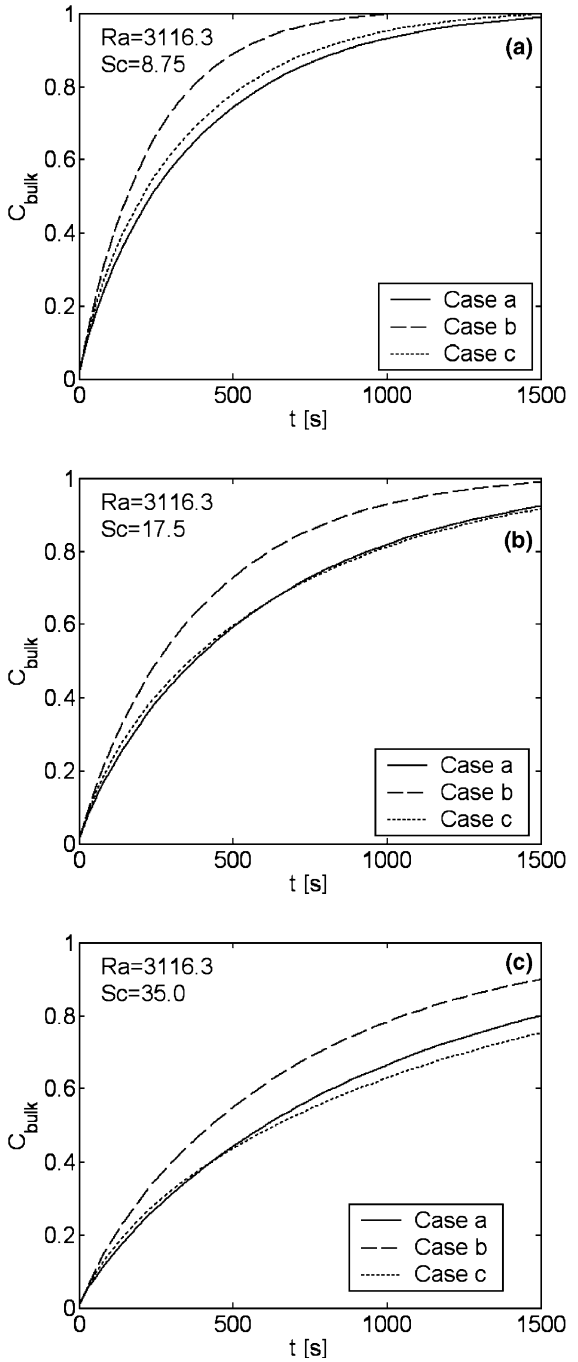

Fig. 7. The bulk (mean or average) oxygen concentration in the liquid as a function of time for temperature boundary conditions (a), (b) and (c) at $Ra = 3116.3$. (a) $Sc = 8.75$; (b) $Sc = 17.5$; and (c) $Sc = 35.0$.

our computational methods. In case (c), there is a small difference in the concentrations in positions 1 and 2 at the early mixing. The difference is negligible after a few hundred seconds (see Fig. 9). Therefore, this design allows us to calibrate two sensors under the same conditions and at the same time. In this way, it is good for us to compare the consistence of the sensors of the same design and compare the difference of the sensors of the

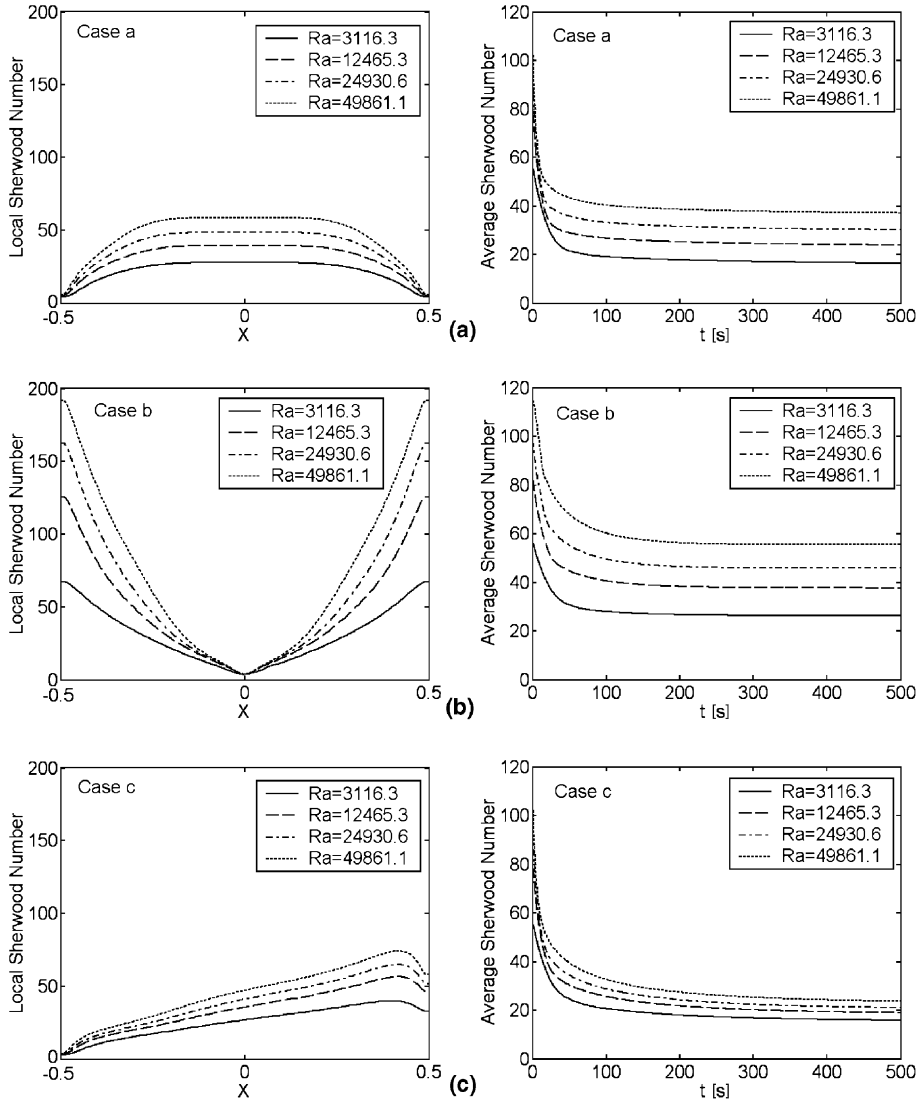

Fig. 8. The local (at $t = 33.8$ s) (left panels) and average Sherwood numbers (right panels) at the interface of the gases and the liquid for different Ra under temperature boundary conditions (a), (b) and (c).

different designs. At positions 1 or 2, under condition (b), it only takes about $t = 1000$ s for the oxygen to reach equilibrium at $Ra = 3116.3$ and $Sc = 17.5$, which is $\sim$90% of the oxygen concentration from the cover gas. Under conditions (a) and (c), it will take slightly longer time to reach the equilibrium. These times are much shorter than the characteristic pure diffusion time t_d ($\sim 10^6$ s) if L is 0.1 m.

In the real experiments, the temperature difference of the hotter and lower walls would be larger than what we chose in our current calculations for ensuring the laminar flow. Higher temperature differences induced stronger natural convections may cause turbulent flows for oxygen transfer. The turbulent mixing is in general faster than the laminar mixing. However, our current analysis determines a threshold for the equilibrium time for oxygen mixing in the system.

4. Conclusion

The numerical analysis of the natural convection driven oxygen transfer in the liquid lead and LBE is presented in this work for three temperature boundary conditions. The simulation results show that the natural convections induced by all the boundary conditions greatly enhance the oxygen transport in the liquid metal of our system. The most efficient one is under tempera-

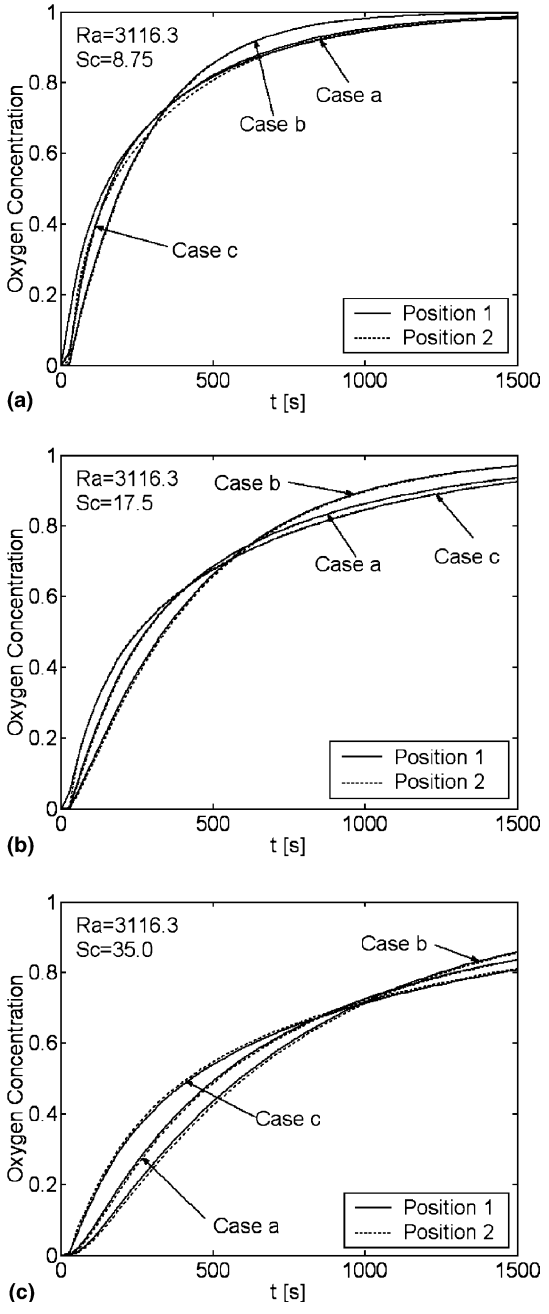

Fig. 9. Oxygen concentrations at sensor locations (see Fig. 1c) for temperature boundary conditions (a), (b) and (c) at $Ra = 3116.3$. (a) $Sc = 8.75$; (b) $Sc = 17.5$; and (c) $Sc = 35.0$.

ture condition (b), in which the sidewalls of the enclosure are heated and the top wall is cooled. It takes about ~1000 s for the oxygen concentration in the whole field to reach ~90% of the input concentration from the top at $Ra = 3116.3$ and $Sc = 17.5$. The pure diffusion would take 10^6 s.

Acknowledgment

The authors would like to thank the financial support from DOE TRP program.

References

[1] Y. Gohar, J. Herceg, L. Krajtl, D. Pointer, J. Saiveau, T. Sofu, P. Finck, Lead–bismuth-eutectic spallation neutron source for nuclear transmuter, ANS 2001 Winter Meeting, Reno, NV (US), 2001.
[2] J.V. Cathcart, W.D. Manly, A technique for corrosion testing in liquid lead, Oak Ridge National Lab. Report, ORNL-1737, 1954.
[3] J. Zhang, N. Li, Y. Chen, A.E. Rusanov, Corrosion behaviors of US steels in flowing lead–bismuth eutectic (LBE), J. Nucl. Mater. 336 (2005) 1–10.
[4] R.S. Lillard, C. Valot, M.A. Hill, P.D. Dickerson, R.J. Hanrahan, The influence of pre-oxidation on the corrosion of steels in liquid lead bismuth eutectic, Los Alamos National Laboratory Report, LA-UR-03-5045, 2003.
[5] G. Müller, A. Heinzel, G. Schumacher, A. Weisenburger, Control of oxygen concentration in liquid lead and lead–bismuth, J. Nucl. Mater. 321 (2003) 256–262.
[6] T.W. Darling, N. Li, Oxygen concentration in liquid Pb–Bi eutectic, Los Alamos National Laboratory Technical Report, LA-UR-02-3036, 2002.
[7] R. Selver, Y. Kamotani, S. Ostrach, Natural convection of a liquid metal in vertical circular cylinders heated locally from the side, J. Heat Transfer 120 (1998) 108–114.
[8] E. Bilgen, X. Wang, P. Vasseur, F. Meng, L. Robillard, On the periodic conditions to simulate mixed convection heat transfer in horizontal channels, Numer. Heat Transfer, Part A 27 (1995) 461–472.
[9] I.E. Sarris, I. Lekakis, N.S. Vlachos, Natural convection in a 2D enclosure with sinusoidal upper wall temperature, Numer. Heat Transfer, Part A 42 (2002) 513–530.
[10] A. Juel, T. Mullin, H.B. Hadid, D. Henry, Three-dimensional free convection in molten gallium, J. Fluid Mech. 436 (2001) 267–281.
[11] H.H.S. Chu, S.W. Churchill, C.V.S. Patterson, The effects of heater size, location, aspect ratio, and boundary conditions on two-dimensional, laminar natural convection in rectangular channels, ASME J. Heat Transfer 98 (1976) 194–201.
[12] M.L. Chadwick, B.W. Webb, H.S. Heaton, Natural convection from two-dimensional discrete heat sources in a rectangular enclosure, Int. J. Heat Mass Transfer 34 (7) (1991) 1679–1693.
[13] R. Viskanta, D.M. Kim, C. Gau, Three-dimensional natural convection heat transfer of a liquid metal in a cavity, Int. J. Heat Mass Transfer 29 (3) (1986) 475–485.
[14] N. Li, Active control of oxygen in molten lead–bismuth eutectic systems to prevent steel corrosion and coolant contamination, J. Nucl. Mater. 300 (2002) 73–81.
[15] J. Zhang, N. Li, Review of studies on fundamental issues in LBE corrosion, Los Alamos National Laboratory Report, LA-UR-04-0869, 2004.

[16] S.S. Kutteladze, V.M. Borishanskii, I.I. Novikov, O.S. Fedynskii, Liquid-metal Heat Transfer Media, Chapman and Hall, 1959, p. 5.
[17] J.P. Holman, Heat Transfer, eighth ed., The McGraw-Hill Companies, Inc, 1997, pp. 360–365.
[18] A.Y. Gelfgat, Convection-induced enhancement of mass transfer through an interface separating two immiscible liquids in a two-lay horizontal annulus, Phys. Fluids 15 (3) (2003) 790–800.
[19] T. Tagawa, H. Ozoe, Effect of Prandtl number and computational schemes on the oscillatory natural convection in an enclosure, Numer. Heat Transfer, Part A 30 (1996) 271–282.
[20] J.C. Tannehill, D.A. Anderson, R.H. Pletcher, Computational Fluid Mechanics and Heat Transfer, second ed., Taylor and Francis Publisher, 1997, pp. 457–459.
[21] R. Selver, Natural Convection of a Liquid Metal in Circular Cylinders Locally Heated from Side Wall, Ph.D. thesis, Case Western Reserve University, 1997.
[22] D.C. Kuo, Application of spectral methods for simulation transport phenomena, Ph.D. thesis, The University of Texas at Austin, 1996.